Ultrafast resonant soft x-ray diffraction dynamics of the charge density wave in TbTe₃

R. G. Moore,[1,*] W. S. Lee,[1,†] P. S. Kirchman,[1] Y. D. Chuang,[2] A. F. Kemper,[1,3] M. Trigo,[1,4] L. Patthey,[1,5] D. H. Lu,[6]
O. Krupin,[7,8] M. Yi,[1] D. A. Reis,[1,4] D. Doering,[2] P. Denes,[2] W. F. Schlotter,[8] J. J. Turner,[8] G. Hays,[8] P. Hering,[8] T. Benson,[8]
J.-H. Chu,[9] T. P. Devereaux,[1] I. R. Fisher,[9] Z. Hussain,[2] and Z.-X. Shen[1,‡]

[1]*Stanford Institute for Materials and Energy Sciences, SLAC National Accelerator Laboratory, Menlo Park, California 94025, USA*
[2]*Advanced Light Source, Lawrence Berkeley National Laboratory, Berkeley, California 94720, USA*
[3]*Lawrence Berkeley National Laboratory, Berkeley, California 94720, USA*
[4]*Stanford PULSE Institute for Ulatrafast Energy Science, SLAC National Accelerator Laboratory, Menlo Park, California 94025, USA*
[5]*Swiss Light Source, Paul Scherrer Institut, CH-5232 Villigen-PSI, Switzerland*
[6]*Stanford Synchrotron Radiation Lightsource, SLAC National Accelerator Laboratory, Menlo Park, California 94025, USA*
[7]*European XFEL, Hamburg, Germany*
[8]*Linac Coherent Light Source, SLAC National Accelerator Laboratory, Menlo Park, California 94025, USA*
[9]*Geballe Laboratory for Advanced Materials and Department of Applied Physics, Stanford University, Stanford, California 94305, USA*

Understanding the emergence of collective behavior in correlated electron systems remains at the forefront of modern condensed matter physics. Disentangling the degrees of freedom responsible for collective behavior can lead to insights into the microscopic origins of emergent properties and phase transitions. Utilizing an optical pump, resonant soft x-ray diffraction probe we are able to track, in real time, the dynamics of the charge density wave (CDW) in TbTe₃, a model system that violates traditional views of a Fermi surface nested CDW. We observe coherent oscillations corresponding to the CDW amplitude mode at 2.4 THz and a coherent optical phonon mode at ∼1.7 THz. We show how such observations reveal the anisotropic energy optimization between in-plane Te charge density modulations and the three-dimensional lattice coupling.

I. INTRODUCTION

Electronic instabilities are at the core of phenomena such as density waves, colossal magnetoresistance, and superconductivity [1–3]. The key to understanding such exotic many-body states is disentangling the contributions from the coupled degrees of freedom. Density waves, of both charge and spin, have been studied for decades and a wealth of information has been gained [1]. While containing interesting properties deserving of attention in their own right, as model systems the insights gained from understanding density-wave phenomena have implications far beyond these material systems themselves. The stripe phase in high-Tc cuprate superconductors, for example, is analogous to a unidirectional charge density wave (CDW) and TbTe₃ under pressure reveals the interplay among superconductivity, magnetic, and charge order [4,5]. However, there are still open questions that need to be resolved for a complete description of the density-wave phenomena. While one-dimensional (1D) systems are well described by Peierls $2k_F$ instabilities [1], this understanding is absent in systems of higher dimensions. For example, there are several existing systems that exhibit prototypical behavior, while traditional theory focusing on Fermi surface (FS) nesting fails to capture the underlying physics [6,7]. The family of the rare-earth tritellurides (RTe₃) is a well-known example of a seemingly prototypical FS nested CDW system but the direction of the CDW is 45° from that predicted by electronic susceptibility calculations at the FS [7–12].

The RTe₃ family crystallizes in the weakly orthorhombic NdTe₃ structure, space group *Cmcm*, consisting of two planar Te nets sandwiched between buckled RTe slabs as shown in Fig. 1(a). The electronic structure near the Fermi energy is dominated by the in-plane Te p_x and p_z orbitals, noting that the *b* axis is the long axis in this structure [7,11–14]. STM and x-ray analysis of TbTe₃ reveal an incommensurate lattice modulation characterized by a single wave vector along the *c* axis ($\mathbf{q}_{CDW} \approx 0.71 \times 2\pi/\mathbf{c}$) at $T = 50$ K [13,15,16]. Angle-resolved photoemission spectroscopy (ARPES) shows a gapped portion of the FS along the CDW direction [11,17]. The temperature dependence of the order parameter follows familiar BCS trends in both x-ray [13] and photoemission [12] data, with a smooth filling-in of the energy gap and correlation lengths orders of magnitude longer than the lattice constants. Heavier rare-earth family members even exhibit a second CDW that once again gaps the FS despite an already reconstructed electronic structure from the first CDW [12]. Time-resolved ARPES (tr-ARPES) shows that the gap is intrinsically linked to the CDW amplitude mode, a collective excitation corresponding to a modulation of the CDW amplitude from its equilibrium value, which is at the core of CDW physics [17–22].

With extensive experimental results illustrating intricate details of the CDW state, a theoretical model describing the underlying microscopic mechanisms remains elusive. By modeling a square Te net, Yao *et al.* [4] demonstrated that due to the underlying quasi-one-dimensionality of the Te bands a unidirectional CDW is favored, but LDA calculations by Johannes *et al.* [7] show the CDW wave vector to be rotated 45° from the direction predicted by the electronic susceptibility, which focuses only on contributions from the FS. When the complete band structure is accounted for, then the correct wave
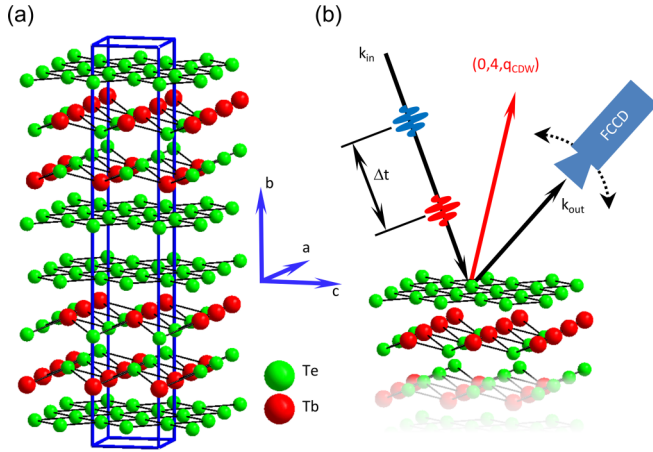

FIG. 1. (a) Crystal structure of TbTe$_3$ with the unit cell outlined in blue. (b) Experimental geometry of the optical pump (red), resonant soft x-ray probe (blue) technique.

vector is predicted. However, there is no divergence or large response in the susceptibility as one would expect from a low-dimensional material: only a small enhancement. Such discrepancies led the authors to conclude that the FS plays little role, if any, in the formation of the CDW state [7].

A focusing effect due to electron-phonon interactions has been invoked to explain the more robust nature of the CDW in two dimensions [4,23,24]. For example, it has been argued that the next-nearest-neighbor hopping between Te atoms that lifts the band degeneracy at the FS p_x and p_z band crossings can create a focusing effect on electron-phonon coupling favoring the crystalline axis of the unit cell and thus the observed CDW direction [24]. Inelastic x-ray scattering has confirmed a momentum-dependent electron-phonon coupling that favors the observed q_{CDW} [25]. Time-resolved electron diffraction measurements also show anisotropy between the a and the c axis which further demonstrates the importance of electron-phonon coupling even along the different in-plane crystalline axes [26].

Here we report time-resolved resonant soft x-ray diffraction experiments in TbTe$_3$ to directly examine the interplay between lattice and charge degrees of freedom in the formation of the CDW state. The diffraction peak resulting from the long-range CDW order was monitored while optically exciting the material. Coherent oscillations were observed at 2.4 and 1.7 THz which can be assigned to the CDW amplitude mode and a lattice optical phonon, respectively, indicating the strongly coupled nature of the charge and lattice degrees of freedom in the CDW state. By considering the atomic motions of the optical phonon mode, shown to mix with the amplitude mode [19,20,27], and the lattice strain induced by atomic motions along different FS nesting vectors, we are able to show how anisotropic lattice strain energy favors CDW formation along the experimentally observed q_{CDW}.

II. EXPERIMENTAL DETAILS

Single crystals of TbTe$_3$ were grown by slow-cooling a binary melt as described elsewhere [13,28]. The CDW phase transition temperature for TbTe$_3$ is approximately 340 K. The
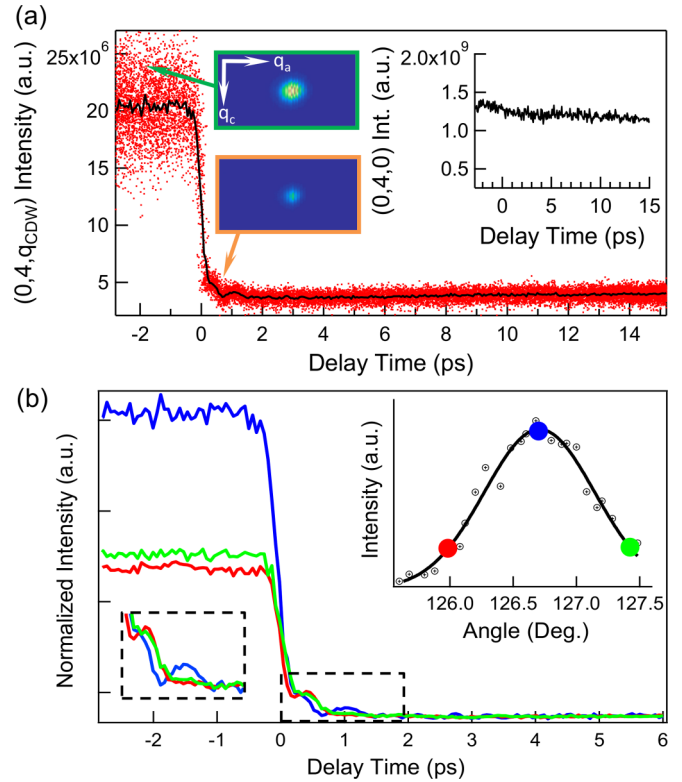

FIG. 2. (a) Experimental data normalized to incident photon flux showing the time dynamics of the $(0,4,q_{CDW})$ diffraction peak and the $(0,4,0)$ Bragg peak (inset). Red points are data from every LCLS, shot while the black line shows averaged data within 60-fs-wide time bins. Inset: fCCD images from a single LCLS shot before and after time 0. (b) Normalized data for different diffraction angles depicted in the top-right rocking curve inset. Lower-left inset: Dashed region of the spectra showing the shift in coherent oscillation peaks resulting from dispersion of coherent modes.

crystals were oriented along the [010] direction using Laue diffraction and cleaved prior to insertion into the vacuum chamber. The sample was then cooled to ≈ 50 K for the measurements.

Time-resolved soft x-ray resonant diffraction experiments were performed using the RSXS end station at the SXR instrument of the Linac Coherent Light Source (LCLS) [29,30]. The dynamics of the $(0,4,q_{CDW})$ diffraction peak were measured while optically pumping at 3 mJ/cm^2 with a 50-fs, 800-nm laser pulse generated utilizing a Ti:sapphire laser amplifier system as schematically shown in Fig. 1(b). The LCLS was operated in the high-charge (250-pC, 70-fs) mode at a 60-Hz repetition rate, and a diffraction image for every shot was recorded by a compact fast x-ray CCD (fCCD) camera, with representative images shown in Fig. 2(a) [31]. Then x-ray absorption spectrum measurements of the Tb M$_5$ edge were used to calibrate the x-ray energy. The photon energy of the x-ray probe pulse was set to the Tb M_5 edge corresponding to the $3d - 4f$ transition in Tb. It should be noted that the diffraction peak due to a CDW modulation in the Te planes is observed while resonantly exciting an electronic transition in the Tb atoms of neighboring planes, as the Tb atoms feel the electrostatic modulation by the Te density wave [32].
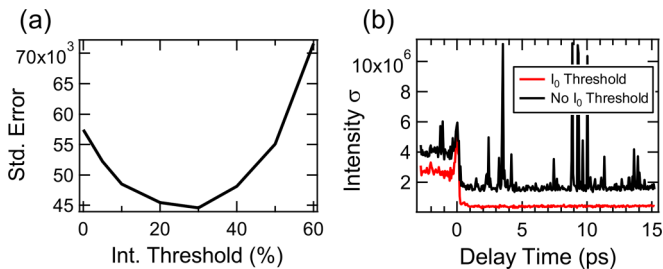
FIG. 3. (a) Standard error for all LCLS shots before time 0 for a particular I_0 threshold. (b) Comparison of the standard deviation for all diffraction intensity measurements within a particular delay time bin with and without I_0 thresholding. The data without thresholding in (b) are shifted vertically upward for clarity.

Each LCLS shot was normalized by the incident photon flux (I_0) as measured by the photocurrent generated from an in-line aluminum foil. A mechanical delay stage with encoded position readout was used to adjust the delay time between the laser pump–x-ray probe pulses. A phase cavity was utilized to correct for the inherent LCLS timing jitter, resulting in an ≈300-fs timing resolution [33]. A fCCD dark frame was generated by averaging ~200 images taken with the LCLS x-ray shutters closed and subtracted from every fCCD image. The diffraction peak intensity was measured by integrating a region 150 × 150 pixels wide centered around the peak.

Due to monochromatization of the x-ray beam, any energy jitter from the LCLS results in an x-ray intensity jitter on the sample. The fCCD camera has inherent thermal and electronic noise and the weak x-ray pulses, with small I_0, will amplify these noise fluctuations during normalization. A critical component in analyzing the data is to create an I_0 threshold to eliminate the weaker x-ray intensity outliers, which can degrade the signal-to-noise ratio and distort the data. Figures 3(a) and 3(b) show the implications of the I_0 thresholding. To determine the appropriate I_0 threshold, the standard error for all LCLS shots prior to time 0 was calculated for different threshold levels as shown in Fig. 3(a). Since the peak intensity is expected to be static prior to 0, minimizing the standard error will maximize the signal-to-noise ratio. Setting the threshold too high will eliminate too many shots and statistical fluctuations will degrade the resulting data. It should be noted that eliminating ≈20%−30% of the weaker x-ray pulses is a good rule of thumb for the unseeded LCLS shots when measuring with an fCCD. The data above the threshold are normalized and then binned according to their jitter-corrected delay time. All shots are averaged within each time bin as shown in Fig. 2(a). Different time-bin widths were considered and yielded similar results as shown below, thus a 60-fs time bin was typically used for the analysis.

III. RESULTS

A. Diffraction peak dynamics

Upon inspection of Fig. 2(a) the slow recovery time, of the order of ~1 ns when modeled with a single exponential (see the Appendix), is immediately apparent while the CDW diffraction peak is still observed after pumping. The observed diffraction peak after the arrival of the pump pulse, which we define
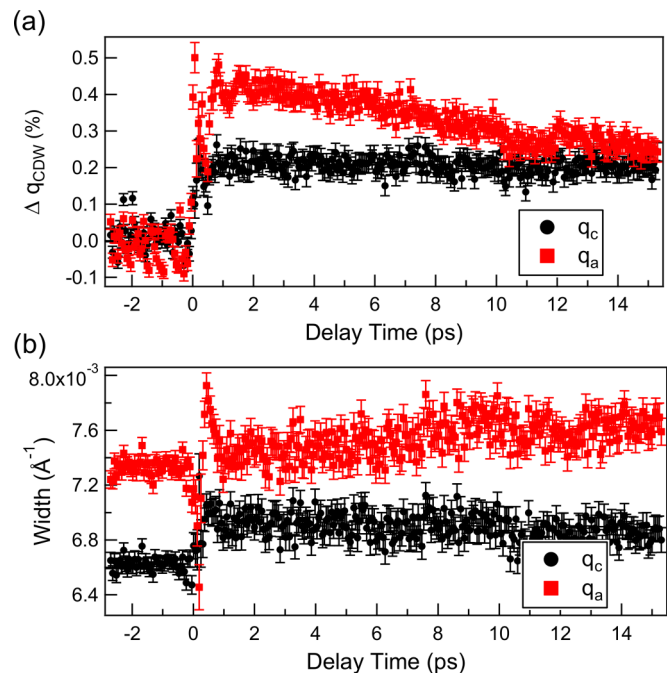

FIG. 4. (a) Relative change in peak position from the 2D Lorentzian fit. (b) Change in diffraction peak width from the 2D Lorentzian fit. Error bars are based on pixel-by-pixel counting statistics and a weighted Lorentzian fit. It should be noted that q_c is along the crystalline c axis, in the direction of q_{CDW}, while q_a is along the a axis, orthogonal to q_{CDW}.

as time 0, could be a finite volume artifact due to the larger, ~60-nm probe depth compared to the estimated ~35-nm pump depth. It should be emphasized that the recovery time observed in Fig. 2 is orders of magnitude longer than the few-picosecond recovery observed in other time-resolved measurements with similar pump fluences [18,19,26]. While the larger probe depth could skew the observed recovery times slightly, it is unlikely to account for the orders-of-magnitude difference. The lack of significant width change in the diffraction peak shown in Fig. 4(b) suggests that the difference between our observed recovery time and previous results is likely due to phase fluctuations as observed in other charge-ordered materials [29]. These incoherent CDWs can depress the diffraction intensity but cannot be detected by previous dynamics experiments that measure only the gap and thus the CDW amplitude. However, since the resonant x-ray process involves transitions between occupied and unoccupied Tb $4f$ multiplets, the pump could also alter the occupation level of these multiplets, resulting in a suppression of the diffraction intensity and overestimation of the CDW recovery time [32].

Previous x-ray diffraction experiments have observed a slight change in q_{CDW} ($\Delta q_{CDW} \sim 1.4\%$) with the temperature near the CDW transition [13]. To measure whether q_{CDW} changes in the pump-probe process, data were taken at detector angles on each side of the rocking-curve maximum as shown in Fig. 2(b). Any changes in q_{CDW} would result in a shift of the rocking curve, resulting in an anisotropy in the spectra from each side of the rocking-curve maximum. The anisotropy in the spectra on each side of the rocking curve is shown

in Fig. 2(b) and is considered negligible. In addition, as the CDW peak is not resolution limited by the fCCD pixels, a shift of q_{CDW} would also cause a change in the peak position on the fCCD detector. Two dimensional Lorentz functions were fit to the averaged fCCD image for each delay time as shown in Figs. 4(a) and 4(b). The shift in the diffraction peak observed in the fCCD image translates into a maximum 0.4% change in q_{CDW} and the width of the diffraction peak shows a negligible change after pumping. As emphasized in the Fig. 2(b) inset, there is a shift of the coherent oscillation peaks in the spectra between the rocking-curve maximum and the two sides which is likely due to the dispersion of the coherent modes, reminiscent of the dispersion of coherent phonons [34]. Unfortunately, the reduction in the signal-to-noise ratio off the rocking-curve maximum precludes any quantitative analysis in the current data. Future experiments with improved statistics or different techniques would likely make such a dispersion measurement possible [35].

While q_{CDW} and the width of the diffraction peak show little change after pumping, oscillation in both of these fit parameters is observed for delay times <2 ps as shown in Figs. 4(a) and 4(b). These oscillations are well above the noise level and suggest a time-dependent and/or frequency-dependent q_{CDW} and coherence length of the CDW order. Future experiments with improved statistics will quantify such trends. In this report, we focus on analyzing the coherent oscillations observed in the CDW diffraction peak intensity.

B. Data fitting and Fourier analysis

For the first few picoseconds after time 0 intensity oscillations are observed. No oscillations are observed in the time dynamics of the (0,4,0) lattice Bragg peak shown in the Fig. 2(a) inset, suggesting that the oscillations are coherent modes intrinsically linked to the underlying CDW state. To better evaluate the coherent modes, a smooth background is subtracted from averaged data as detailed in the Appendix. The pronounced decrease in the diffraction intensity after time 0 and the sloping background at later delay times preclude Fourier transformation of the transient diffraction intensity directly and necessitates subtraction of the phenomenological background. The goal is to obtain an oscillatory trace without step-like features or slow variations and thus enable a clear identification of the coherent modes in the Fourier spectrum.

In the Appendix we show that by performing various Fourier transformations the coherent modes are independent of details of the phenomenological background, the size of the time bins, and the window being Fourier-transformed, which highlights the robustness of our observations. The experimental results used for our physical interpretation are summarized in Figs. 5 and 6.

While the residual intensity oscillations are near the noise level they are still resolved, even in the raw data in Fig. 2(a). The Fourier-transformed amplitudes within a 0- to 4-ps window show three peaks above the background. We assign the peak centered at $\sim$2.4 THz to be the amplitude mode of the CDW in agreement with other experiments [17,19,20,27]. Lattice modes with similar energies have been observed in other measurements but no coherent oscillations appear in the lattice Bragg peak as shown in the Fig. 2(a) inset, and one
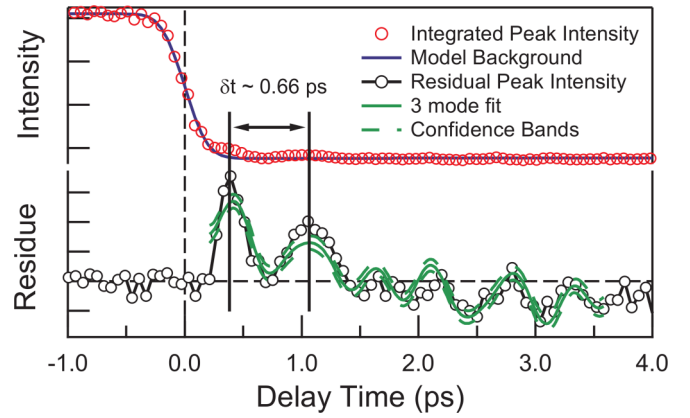

FIG. 5. Normalized data and background fit (top) and residual intensity after background subtraction with a three-mode sinusoidal fit (bottom).

would expect the amplitude mode to be a dominant feature in the CDW diffraction peak dynamics [19,20,25,27]. In addition, there are two large peaks in Fig. 6 near 1.2 and 1.7 THz. The distance between the peaks of the first two oscillations is $\sim$0.66 ps and $\sim$1.5 THz as shown in Fig. 5 which is consistent with the dominant Fourier-transformed peaks in Fig. 6 but also suggests that these features could be one single mode distorted by the limited resolution and number of oscillations observed. To check the Fourier transform results, the residual data were fit with a three-sinusoidal-mode model as shown in Fig. 5. The model fit frequencies and amplitudes are consistent with those from the Fourier transform analysis as shown in Fig. 6.

C. Theoretical mode analysis

To understand the origins of the observed modes, density functional theory calculations were performed using the Quantum ESPRESSO [36] package (version 5.0) with ultrasoft pseudopotentials. We used the Perdew-Burke-Ernzerhof [37]
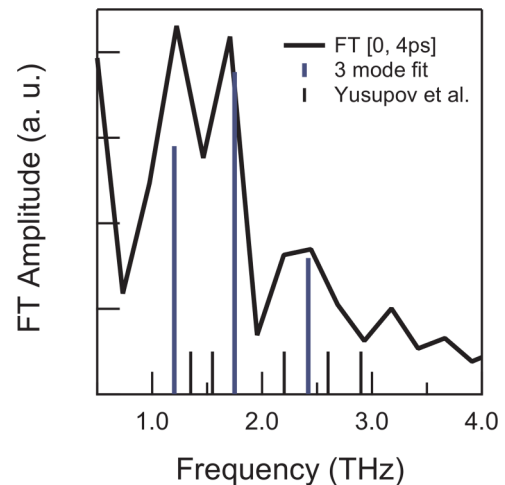

FIG. 6. Fourier transform amplitude for a $0 - 4$ ps time window of the residual intensity data. Vertical bars represent frequency and amplitude of three mode sinusoidal fit and reflectivity measurements from Ref. [20].
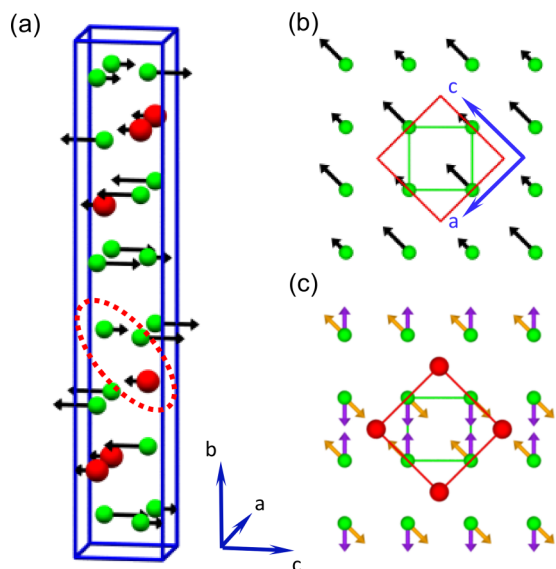
FIG. 7. (a) Calculated atomic displacements of the 1.7-THz mode. Arrows lengths are proportional to displacement. The dotted (red) oval emphasizes the interaction of Te motion constrained by the neighboring Tb layer. (b) Te motions within a single Te layer resulting from the out-of-plane interactions. The central (green) square outlines the 2D Te net and the larger, tilted (red) square outlines the 3D crystal unit cell. (c) Atomic motions for the total energy calculations in Fig. 9 for the different nesting directions.

formulation for the exchange-correlation functional within GGA. To obtain the energies of the phonon modes, we performed calculations of the dynamical matrix with a kinetic energy cutoff of 500 eV and a $13 \times 3 \times 13$ momentum grid for the plane-wave basis. Energies were converged with respect to the number of k points and both the wave-function energy cutoff and the density energy cutoff converged to 30 meV. The dynamical matrix was subsequently diagonalized to obtain the eigenmodes of atomic displacements. Time-resolved reflectivity and Raman data suggest that the 1.7-THz mode is a lattice phonon mode that mixes with the CDW amplitude mode at $T \approx 250$ K [19,20,27]. Thus we assume that the 1.7-THz mode is a normal-state optical phonon mode and identify the atomic displacements, shown in Fig. 7, by noting the resulting frequencies of oscillation and their trends as both the momentum grid and the energy cutoff are increased. The 1.2-THz mode is harder to identify, as there are several modes similar in energy as shown in Fig. 8. Due to the ambiguity in mode assignment and lack of observed mixing with the CDW amplitude mode the 1.2-THz mode is not a focus in this work.

To investigate the relative cost in strain between the two proposed directions of atomic motion in the CDW, i.e., along the 001 and 101 directions (as shown by the orange and purple arrows, respectively, in Fig. 7), we performed single-point total energy calculations for a $2 \times 2 \times 1$ (3D) supercell as a function of the displacement distance. We created a $q = 0$ distortion of the unit cell along the indicated displacement pattern and displaced the involved atoms an equal amount. Since the CDW is incommensurate, it is difficult to create a supercell large enough to model atomic distortions modulated by the observed q vector. This calculation assumes that all the atoms participating in the CDW are displaced by the
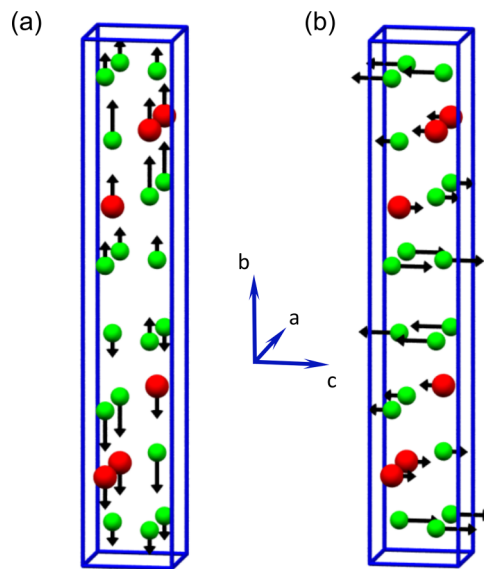

FIG. 8. Potential candidates for the observed 1.2-THz mode. (a) Mode with the calculated energy closest to the observed 1.2 THz. (b) Doubly degenerate mode (motions along either the *a* or the *c* axis) with the calculated energy of 1.1 THz.

full amount, leading to an ordering vector in the calculation which is shorter than experimentally observed. As a result, the absolute scale of the displacement energy is overestimated compared to the CDW energy. Nevertheless, the comparison between the two directions is still valid. Our calculations show that the cost of atomic displacement along the 101 (purple) direction is higher than along the 001 (orange) direction as shown in Fig. 9. This suggests that the presence of the Tb ions causes a steric hindrance in the 101 direction and changing the ordering vector to the experimentally observed one costs less in energy.
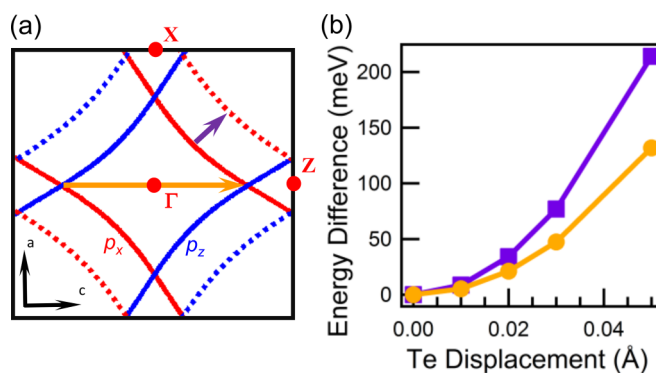

FIG. 9. (a) Tight-binding model of the Fermi surface in the first Brillouin zone. Solid red (blue) lines are the p_x (p_z) bands from the 2D Te net, and dashed lines are 2D Te bands folded back into the reduced Brillouin zone due to weak 3D potentials. The horizontal (orange) arrow shows the CDW nesting vector realized in the material and the short (purple) arrow represents the electronic susceptibility maximum from LDA calculations at the Fermi surface [7]. (b) Total energy difference calculated for Te displacements along the orange and purple nesting directions in Fig. 7(c). The results show that displacements along the c axis cost less in energy.

IV. DISCUSSION

The mode frequencies shown in Fig. 6 agree remarkably well with previous tr-ARPES [17,22], Raman [27], and reflectivity [20] experiments. This agreement gives us confidence in the Fourier transform analysis and mode assignment despite the limited number of oscillations and signal-to-noise limitations. Both Raman and reflectivity data observe the ~1.7-THz mode and show that it mixes with the amplitude mode at a temperature just below the CDW T_c and thus is the focus of our discussion [20,27]. The mode that best fits the experimental frequency is the optical mode shown in Fig. 7(a). It is not surprising that all the atoms within the unit cell move in concert as part of the eigenmode. What is surprising is the level of interaction between the Te and the Tb motions revealed in the phonon calculations graphically expressed as different arrow lengths for different Te atoms in Fig. 7(a). While it is a layered system, the interlayer coupling between the Te and the neighboring Tb planes nevertheless creates site-dependent motions of Te atoms within the CDW plane. Figure 7(b) emphasizes this anisotropy, depicted as different arrow lengths for atoms within the same Te plane. To understand the implications of these site-dependent motions, we need to understand how atomic displacements connect to the nested FS shown in Figs. 7(c) and 9(a). Assuming an in-plane longitudinal density wave, the total energy for Te displacements along the different nesting directions in Fig. 9(a) is calculated and shown in Fig. 9(b). The interlayer coupling resulting in the large anisotropy for the Te motions within the CDW plane translates into a large anisotropy in total energy for a strained lattice in the different nesting directions. The ideal nesting direction based on the shape of the FS [purple arrow in Fig. 9(a)] costs more in strain energy due to the buckled RTe slab. Such a large anisotropy in lattice coupling and strain energy implies a large anisotropy in the electron-phonon coupling. The CDW ground state is the result of an energy minimization and the energy reduction in the electronic structure must be balanced with the lattice strain energy incurred.

Previous works have demonstrated that there exists an interplay between the 1.7-THz mode and the CDW amplitude mode [20,27]. The simple fact that the 1.7-THz mode appears as a dominant feature in the time-resolved dynamics of the CDW diffraction data suggests that it has an important relation to the CDW amplitude mode and possibly the underlying CDW mechanisms. The interplay and mixing between the 1.7-THz mode and the amplitude mode demonstrate the importance and directionality of coupling between lattice motions and the electronic instability imposed by the electronic structure. Such anisotropy in electron-phonon coupling and strain energy is not accounted for in traditional susceptibility calculations at the FS. Previous studies have observed anisotropic electron-phonon coupling in these materials [24–26], but our results yield new insights into the origins of the anisotropy and the delicate energy balance that creates the broken-symmetry ground state.

It is common to find layered materials exhibiting emergent behavior with large unit cells encompassing many layers. The large 3D structures result in potentials that fold electronic bands back into reduced Brillouin zones, but the folding potentials are often weak, resulting in electronic structures that are still highly 2D. While band folding creates an ideal FS nesting condition in TbTe$_3$, the buckled TbTe slab is viewed as a simple charge reservoir determining the Fermi level but having few implications for the dimensionality of the electronic structure [11]. In contrast, the electronic structure may appear 2D but phonon modes still involve the entire 3D lattice. While charge density modulations exist in the Te plane [15,38] and the amplitude mode is connected to oscillations of the gapped in-plane p_x and p_z bands, the strain energy and electron-phonon coupling are significantly different between the c axis and the 45° nesting directions.

V. CONCLUSIONS

We have measured the time-resolved diffraction dynamics of lattice distortions resulting from the CDW order in TbTe$_3$. We observed coherent oscillations from the CDW amplitude mode at 2.4 THz and from a lattice optical phonon at 1.7 THz. Theoretical investigations resolve the atomic motions of the 1.7-THz phonon and show how the motions of atoms within the Te plane are dramatically affected by the neighboring Tb atoms. Calculations of the lattice strain energy show that Te displacements along the direction that best nests the electronic FS cost more in energy than displacements that nest the second-best region of the FS. Our results emphasize the importance of lattice strain energy and anisotropy when determining the ground state of systems with coupled degrees of freedom.

APPENDIX: BACKGROUND SUBTRACTION AND FOURIER ANALYSIS

In the following we detail what steps were taken to ensure that the resulting Fourier spectrum is independent of the details of the model background, the size of the time bins the raw data
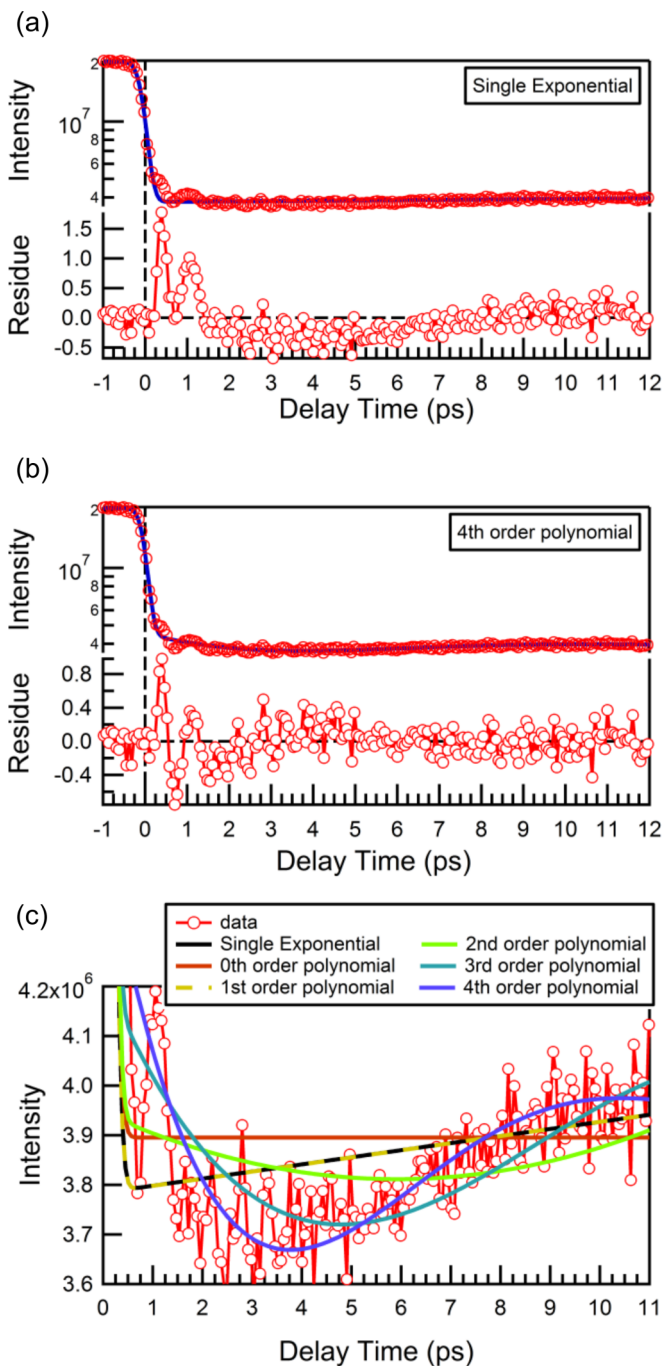
(a)

(b)

(c)

FIG. 10. (a) Background subtraction of a single exponential according to Eq. (A2). (b) Fourth-order polynomial background subtraction after Eq. (A1). Background subtraction performed on the data set with 60-fs bins. Please note that the diffraction intensity is plotted on a logarithmic scale to enhance the visibility of the small oscillations. (c) Comparison of different models for background subtraction with a focus on the low-intensity region after the initial step.
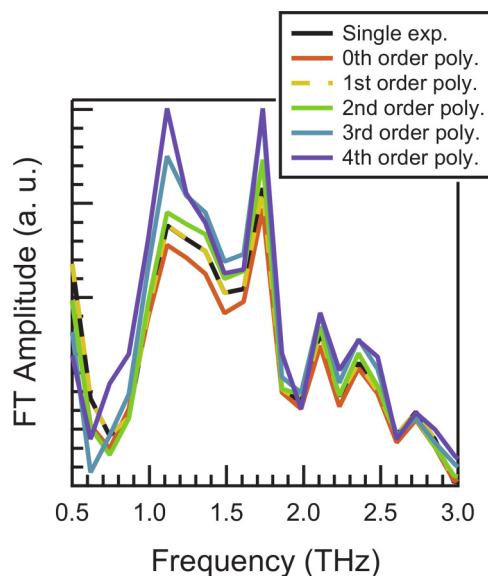

FIG. 11. Fourier transforms of the residuals for different model backgrounds for 60-fs bins and a time window ranging from 0 to 8 ps, which corresponds to a nominal frequency resolution of 0.13 THz.

using a Gaussian error function with full width half-maximum w. The time delay when the intensity has dropped to half of its initial equilibrium value is given by t_0 and defines time 0 in our experiments. We investigated polynomial backgrounds up to fourth order N [Eq. (A1)] and single-exponential recovery of the diffraction intensity with a time constant τ [Eq. (A2)]. Here, a_i are free parameters of the fits:

$$\mathrm{BG}_{\mathrm{poly}}(t) = \left(\sum_{i=0}^{N} a_i (t-t_0)^i \right) \left(1 + \mathrm{erf}\left(\frac{2\sqrt{2}(t-t_0)}{w} \right) \right) \Big/ 2, \tag{A1}$$

$$\mathrm{BG}_{\mathrm{exp}}(t) = (a_0 + a_1 \exp\left(-(t - t_0)/\tau\right))$$
$$\times \left(1 + \mathrm{erf}\left(\frac{2\sqrt{2}(t - t_0)}{w} \right) \right) \Big/ 2. \tag{A2}$$

(a)   (b)
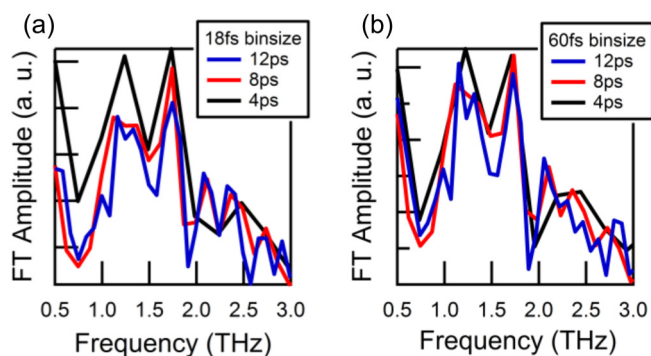
FIG. 12. Comparison of Fourier transforms for different bin sizes and increasing lengths of the time windows. The nominal frequency resolution in frequency space is indicated. (a) Bins 18-fs width. (b) Bins of 60-fs width.

are sorted into, and the length of the time window the Fourier transform is applied to. We begin with a discussion of different phenomenological backgrounds. In all investigated models, the suppression of the diffraction intensity after arrival of the pump pulse is modeled by a step function that is calculated

Figure 10 compares different models for background subtraction. All analysis was performed on the data set with a bin size of 60 fs. Due to the slow recovery of the signal on a nanosecond time scale, even the crudest model, which subtracts only a constant background after time 0, is able to extract the coherent oscillations. While increasing the polynomial order generates a smoother residual at later times, it tends to perform suboptimally around the initial step. Figure 10(c) focuses on the behavior of the traces for background subtraction after the initial intensity decrease. Note that due to the slow recovery of the signal the first-order polynomial effectively gives the same result as a single-exponential recovery with the fitted time constant of $\tau = 1160(250)$ ps. While the limited number of data yields a large error in the fit, it is clear that our observed recovery is significantly slower than observed in previous experiments [18,19,26].

Figure 11 depicts the resulting Fourier transforms of the residuals after background subtraction for 60-fs bins and a time window ranging from 0 to 8 ps, which corresponds to a nominal frequency resolution of 0.13 THz. This comparison evidences that details of the background subtraction do not influence the coherent modes we can identify in the Fourier spectrum. We thus chose a single-exponential recovery, which allows us to extract a recovery time constant.

In the next step we investigate the dependence of the Fourier transforms on the bin size, which directly changes the statistics for each data point, and the length of the time window being Fourier transformed, which relates to the nominal frequency resolution in the Fourier spectrum. The results are shown in Fig. 12. Again, the coherent modes can be clearly identified in all traces and do not depend on the choice of bin width and window size.

[1] G. Grüner, *Density Waves in Solids* (Addison-Wesley, Reading, MA, 1994).

[2] E. Dagotto, Science **309**, 257 (2005).

[3] H. Y. Hwang, Y. Iwasa, M. Kawasaki, B. Keimer, N. Nagaosa, and Y. Tokura, Nat. Mater. **11**, 103 (2012).

[4] H. Yao, J. A. Robertson, E.-A. Kim, and S. A. Kivelson, Phys. Rev. B **74**, 245126 (2006).

[5] J. J. Hamlin, D. A. Zocco, T. A. Sayles, M. B. Maple, J.-H. Chu, and I. R. Fisher, Phys. Rev. Lett. **102**, 177002 (2009).

[6] K. Rossnagel, J. Phys. Condens. Matter **23**, 213001 (2011).

[7] M. D. Johannes and I. I. Mazin, Phys. Rev. B **77**, 165135 (2008).

[8] E. DiMasi, M. C. Aronson, J. F. Mansfield, B. Foran, and S. Lee, Phys. Rev. B **52**, 14516 (1995).

[9] G.-H. Gweon, J. D. Denlinger, J. A. Clack, J. W. Allen, C. G. Olson, E. DiMasi, M. C. Aronson, B. Foran, and S. Lee, Phys. Rev. Lett. **81**, 886 (1998).

[10] V. Brouet, W. L. Yang, X. J. Zhou, Z. Hussain, N. Ru, K. Y. Shin, I. R. Fisher, and Z. X. Shen, Phys. Rev. Lett. **93**, 126405 (2004).

[11] V. Brouet, W. L. Yang, X. J. Zhou, Z. Hussain, R. G. Moore, R. He, D. H. Lu, Z. X. Shen, J. Laverock, S. B. Dugdale *et al.*, Phys. Rev. B **77**, 235104 (2008).

[12] R. G. Moore, V. Brouet, R. He, D. H. Lu, N. Ru, J.-H. Chu, I. R. Fisher, and Z.-X. Shen, Phys. Rev. B **81**, 073102 (2010).

[13] N. Ru, C. L. Condron, G. Y. Margulis, K. Y. Shin, J. Laverock, S. B. Dugdale, M. F. Toney, and I. R. Fisher, Phys. Rev. B **77**, 035114 (2008).

[14] J. Laverock, S. B. Dugdale, Z. Major, M. A. Alam, N. Ru, I. R. Fisher, G. Santi, and E. Bruno, Phys. Rev. B **71**, 085114 (2005).

[15] A. Fang, N. Ru, I. R. Fisher, and A. Kapitulnik, Phys. Rev. Lett. **99**, 046401 (2007).

[16] A. Banerjee, Y. Feng, D. M. Silevitch, J. Wang, J. C. Lang, H.-H. Kuo, I. R. Fisher, and T. F. Rosenbaum, Phys. Rev. B **87**, 155131 (2013).

[17] F. Schmitt, P. S. Kirchmann, U. Bovensiepen, R. G. Moore, L. Rettig, M. Krenz, J.-H. Chu, N. Ru, L. Perfetti, D. H. Lu *et al.*, Science **321**, 1649 (2008).

[18] F. Schmitt, P. S. Kirchmann, U. Bovensiepen, R. G. Moore, J.-H. Chu, D. H. Lu, L. Rettig, M. Wolf, I. R. Fisher, and Z.-X. Shen, New J. Phys. **13**, 063022 (2011).

[19] R. Yusupov, T. Mertelj, V. V. Kabanov, S. Brazovskii, P. Kusar, J.-H. Chu, I. R. Fisher, and D. Mihailovic, Nat. Phys. **6**, 681 (2010).

[20] R. V. Yusupov, T. Mertelj, J.-H. Chu, I. R. Fisher, and D. Mihailovic, Phys. Rev. Lett. **101**, 246402 (2008).

[21] L. Rettig, J.-H. Chu, I. R. Fisher, U. Bovensiepen, and M. Wolf, Faraday Discuss. **171**, 299 (2014).

[22] D. Leuenberger, J. A. Sobota, S.-L. Yang, A. F. Kemper, P. Giraldo-Gallo, R. G. Moore, I. R. Fisher, P. S. Kirchmann, T. P. Devereaus, and Z.-X. Shen, Phys. Rev. B **91**, 201106(R) (2015).

[23] T. Kiss, T. Yokoya, A. Chainani, S. Shin, T. Hanaguri, M. Nohara, and H. Takagi, Nat. Phys. **3**, 720 (2007).

[24] H.-M. Eiter, M. Lavagnini, R. Hackl, E. A. Nowadnick, A. F. Kemper, T. P. Devereaux, J.-H. Chu, J. G. Analytis, I. R. Fisher, and L. Degiorgi, Proc. Natl. Acad. Sci. U.S.A. **110**, 64 (2013).

[25] M. Maschek, S. Rosenkranz, R. Heid, A. H. Said, P. Giraldo-Gallo, I. R. Fisher, and F. Weber, Phys. Rev. B **91**, 235146 (2015).

[26] T.-R. T. Han, T. Zhensheng, S. D. Mahanti, K. Chang, C.-Y. Ruan, C. D. Malliakas, and M. G. Kanatzidis, Phys. Rev. B **86**, 075145 (2012).

[27] M. Lavagnini, H.-M. Eiter, L. Tassini, B. Muschler, R. Hackl, R. Monnier, J.-H. Chu, I. R. Fisher, and L. Degiorgi, Phys. Rev. B **81**, 081101(R) (2010).

[28] N. Ru and I. R. Fisher, Phys. Rev. B **73**, 033101 (2006).

[29] W. S. Lee, Y. D. Chuang, R. G. Moore, Y. Zhu, L. Patthey, M. Trigo, D. H. Lu, P. S. Kirchmann, O. Krupin, M. Yi *et al.*, Nat. Commun. **3**, 838 (2012).

[30] W. F. Schlotter, J. J. Turner, M. Rowen, P. Heimann, M. Holmes, O. Krupin, M. Messerschmidt, S. Moeller, J. Krzywinski, R. Soufli *et al.*, Rev. Sci. Instrum. **83**, 043107 (2012).

[31] D. Doering, Y. D. Chuang, N. Andresen, K. Chow, D. Contarato, C. Cummings, E. Domning, J. Joseph, J. S. Pepper, B. Smith *et al.*, Rev. Sci. Instrum. **82**, 073303 (2011).

[32] W. S. Lee, A. P. Sorini, M. Yi, Y. D. Chuang, B. Moritz, W. L. Yang, J.-H. Chu, H. H. Kuo, A. G. Cruz Gonzalez, I. R. Fisher *et al.*, Phys. Rev. B **85**, 155142 (2012).

[33] J. M. Glownia, J. Cryan, J. Andreasson, A. Belkacem, N. Berrah, C. I. Blaga, C. Bostedt, J. Bozek, L. F. DiMauro, L. Fang *et al.*, Opt. Express **18**, 17620 (2010).

[34] A. M. Lindenberg, I. Kang, S. L. Johnson, T. Missalla, P. A. Heimann, Z. Chang, J. Larsson, P. H. Bucksbaum, H. C. Kapteyn, H. A. Padmore *et al.*, Phys. Rev. Lett. **84**, 111 (2000).

[35] M. Trigo, M. Fuchs, J. Chen, M. P. Jiang, M. Cammarata, S. Fahy, D. M. Fritz, K. Gaffney, S. Ghimire, A. Higginbotham *et al.*, Nat. Phys. **9**, 790 (2013).

[36] P. Giannozzi, S. Baroni, N. Bonini, M. Calandra, R. Car, C. Cavazzoni, D. Ceresoli, G. L. Chiarotti, M. Cococcioni, I. Dabo *et al.*, J. Phys. Condens. Matter **21**, 395502 (2009).

[37] J. P. Perdew, K. Burke, and M. Ernzerhov, Phys. Rev. Lett. **77**, 3865 (1996).

[38] H. J. Kim, C. D. Malliakas, A. T. Tomić, S. H. Tessmer, M. G. Kanatzidis, and S. J. L. Billinge, Phys. Rev. Lett. **96**, 226401 (2006).